ESA UNCLASSIFIED - For Official Use

esac

European Space Astronomy Centre (ESAC)
European Space Agency (ESA)
Camino Bajo del Castillo s/n
Urb. Villafranca del Castillo
28692 Villanueva de la Canada - Madrid
SPAIN

# PSA PRODUCT USER GUIDE - BAHIA ET AL (2022) DISCORDANCE VALLEY MAP OF MARS DATA



| | |
|---|---|
| **Prepared by** | **R. S. Bahia** |
| **Reference** | **PUG-ESA_Mars_Valleys_HRSC_CTX** |
| **Issue / Revision** | **1 / 1** |
| **Date of Issue** | **16/08/2022** |



European Space Agency
Agence spatiale européenne

# CHANGE LOG

| Reason for change | Issue | Revision | Date |
|---|---|---|---|
| Initial version | 1 | 0 | 11/17/2019 |
| Second version based on first experience | 1 | 1 | 11/17/2019 |

# CHANGE RECORD

| **Issue** 1 | **Revision** 1 | | |
|---|---|---|---|
| **Reason for change** | **Date** | **Pages** | **Paragraph(s)** |
| Initial version | 03/11/2018 | All | All |
| Few global updates | 06/17/2019 | All | All |
| Added one new section | 01/15/2020 | N/A | §5 |
| Added additional inputs on the instructions to open products | 01/15/2020 | N/A | §4 |

**Table of contents:**

# 1. INTRODUCTION

## 1.1 Executive Summary

This dataset is comprised of shapefiles, georeferenced to the simple cylindrical projection of Mars, hereafter SimpleCylindrical_Mars, of Martian fluvial valley networks mapped using High-Resolution Stereo Camera images (15 – 25 m per pixel) in a pole-to-pole strip located from 20°W - 20°E. The purpose of this dataset is to assess the conformity between valley orientation and surface slope direction. The shapefiles contain the following information:

- valley length (m)
- valley orientation (°)
- average surface slope direction (°), and
- the difference between valley orientation and surface slope direction (°).

This dataset is associated with the following publication:

https://doi.org/10.1016/j.icarus.2022.115041

## 1.2 Extended introduction

In addition to the fluvial valley networks with associated valley orientation and surface slope conformity data, the dataset also contains shapefiles for valleys that were mapped that have unclear origins, and also inverted channels.

Valleys were mapped in ESA's Mars Express High-Resolution Stereo Camera (HRSC) images. In the few places without HRSC coverage, Mars Global Surveyor Context Camera (CTX) images were used. Topographic data, for surface slope direction calculations, were extracted from the NASA's Mars Global Surveyor Mars Orbiter Laser Altimeter (MOLA) global mosaic.

The HRSC images were obtained from the ESA's Planetary Science Archive (PSA):
https://archives.esac.esa.int/psa/ftp/MARS-EXPRESS/HRSC/

The CTX images were obtained from the Mars Space Flight Facility Image Explorer:
http://viewer.mars.asu.edu/viewer/ctx?fbclid=IwAR2GeG5pqU4-2VaVGT96rU05y-cqNzrbnYCqWt8a9j00wKOUCVOEcbxOKSM#T=0

The MOLA data was downloaded from the USGS Astropedia website:
https://astrogeology.usgs.gov/search/map/Mars/GlobalSurveyor/MOLA/Mars_MGS_MOLA_DEM_mosaic_global_463m

## 1.3 Bahia Martian Valley Datasets

Utilising this dataset should be fairly easy for anyone familiar with GIS (Geographical Information Systems) software. All data is georeferenced to the SimpleCylindrical_Mars and ready for direct input into any GIS software.

All data (valley length, valley orientation, average surface slope direction, and the difference between valley orientation and surface slope direction) is accessible via the attribute table of the dataset.

The way in which the valleys were mapped and data extraction and calculation was performed is explained in detail in the following publication:

Bahia, R. S., S. Covey-Crump, M. A. Jones and Neil Mitchell (2022), Discordance analysis on a high-resolution valley network map of Mars: Assessing the effects of scale on the conformity of valley orientation and surface slope direction, Icarus, 383, 1150.

Please contact riccibahia@hotmail.com if you require further information about the dataset.

## 1.4 Abbreviations and Acronyms

CTX – Context Camera

DOI - Digital Object Identifier

ESA - European Space Agency

HRSC – High Resolution Stereo Camera

MOLA - Mars Orbiter Laser Altimeter

NASA - National Aeronautics and Space Administration

PSA - Planetary Science Archive

## 1.5 Reference and Applicable Documents

Bahia, R. S., S. Covey-Crump, M. A. Jones and Neil Mitchell (2022), Discordance analysis on a high-resolution valley network map of Mars: Assessing the effects of scale on the conformity of valley orientation and surface slope direction, Icarus, 383, 115041.

Bahia, R. S. and M. Jones (2020), The subjectivity in identification of Martian channel networks and its implication for citizen science projects, Earth Moon Planets, https://doi.org/10.1007/s11038-020-09530-y

Burr, D. M., R. M. E. Williams, K. D. Wendell, M. Chojnacki and J. P. Emery (2010), Inverted fluvial features in the Aeolis/Zephyria Plana region, Mars: Formation mechanism and initial paleodischarge estimates, J. Geophys. Res. Planets, 115, 1-20.

Carr, M. H. (1995), The Martian drainage system and the origin of valley networks and fretted channels, J. Geophys. Res., 100, 7479–7507.

Davis, J. M., M. Balme, P. M. Grindrod, R. M. E. Williams, and S. Gupta (2016), Extensive Noachian fluvial systems in Arabia Terra: Implications for early Martian climate, Geology, 44 (10), 847-850, doi:10.1130/G38247.1

Horton, R. E. (1945), Erosional development of streams and their drainage basins; hydrophysical approach to quantitative morphology, Bull. Geol. Soc. Am., 56, 275–370.

Hynek, B. M., M. Beach and M. R. T. Hoke (2010), Updated global map of Martian valley networks and implications for climate and hydrologic processes, J. Geophys. Res., 115, 1-14.

Lemoine, F.G., Smith, D.E., Rowlands, D.D., Zuber, M.T., Neumann, G.A., Chinn, D.S., Pavlis, D.E. (2001), An improved solution of the gravity field of Mars (GMM-2B) from Mars Global Surveyor, J. Geophys. Res., 106, 23359-23376.

Luo, W. and T. F. Stepinski (2012), Orientation of valley networks on Mars: The role of impact cratering, Geophys. Res. Letters, 39, L24201, doi:10.1029/2012GL054087.

Neukum, G., R. Jaumann & the HRSC Co-Investigator and Experiment Team (2004), HRSC: the High Resolution Stereo Camera of Mars Express, Mars Express: the scientific payload. Ed. by Andrew Wilson, scientific coordination: Agustin Chicarro. ESA SP-1240, Noordwijk, Netherlands: ESA Publications Division, ISBN 92-9092-556-6, 2004, 17 – 35.

Neumann, G. A., D. D. Rowlands, F. G. Lemoine, D. E. Smith, and M. T. Zuber (2001), Crossover analysis of Mars Orbiter Laser Altimeter data, J. Geophys. Res., 106, 23753–23768. https://doi.org/10.1029/2000JE001381

Pilorget, C. and F. Forget (2016), Formation of gullies on Mars by debris flows triggered by CO2 sublimation, Nature Geoscience, 9, 65-69.

Scott, D. H., J. M. Dohm, and J. W. Rice Jr. (1995), Map of Mars showing channels and possible paleolake basins, U.S. Geol. Surv. Misc. Invest. Ser., Map I-1350, 1:30,000,000.

Skinner, J. A., T. M. Hare and K. L. Tanaka (2006), Digital renovation of the atlas of Mars 1: 15,000,000 – scale global geologic series maps, LPSC XXXVII, abstract #2331.

Smith, D. E., M. T. Zuber, H. V. Frey, et al. (2001), Mars Orbiter Laser Altimeter (MOLA): Experiment summary after the first year of global mapping of Mars, J. Geophys. Res., 106, 23689-23722.

Sylvest, M.E., J. C. Dixon, S. J. Conway, M. R. Patel, J. N. McElwaine, A. Hagermann and A. Barnes (2018), CO2 sublimation in Martian gullies: laboratory experiments at varied slope angle and regolith grain sizes, Geological Society, London, Special Publications, 467, 343-371.

Tanaka, K. L., S. J. Robbins, C. M. Fortezzo, J. A. Skinner Jr., and T. M. Hare (2014), The digital global geologic map of Mars: Chronostratigraphic ages, and crater morphologic characteristics, and updated resurfacing history, Planetary and Space Science, 95, 11-24.

Williams, R. M. E, R. P. Irwin III and J. R. Zimbelman (2009), Evaluation of paleohydrologic models for terrestrial inverted channels: Implications for application to Martian sinuous ridges, Geomorphology, 107, 300-315.

## 2. SCIENTIFIC OBJECTIVES

Three SOURCES were used to produce this dataset – HRSC and CTX images and MOLA digital elevation data.

The purpose of the study is to examine the spatial and temporal evolution of the Martian surface by slope discordance mapping of channels and valleys that were formed, either directly or indirectly, by precipitation. **Discordance** is defined as the difference between valley orientation and the surrounding topographic surface slope direction of steepest descent (Figure 1).

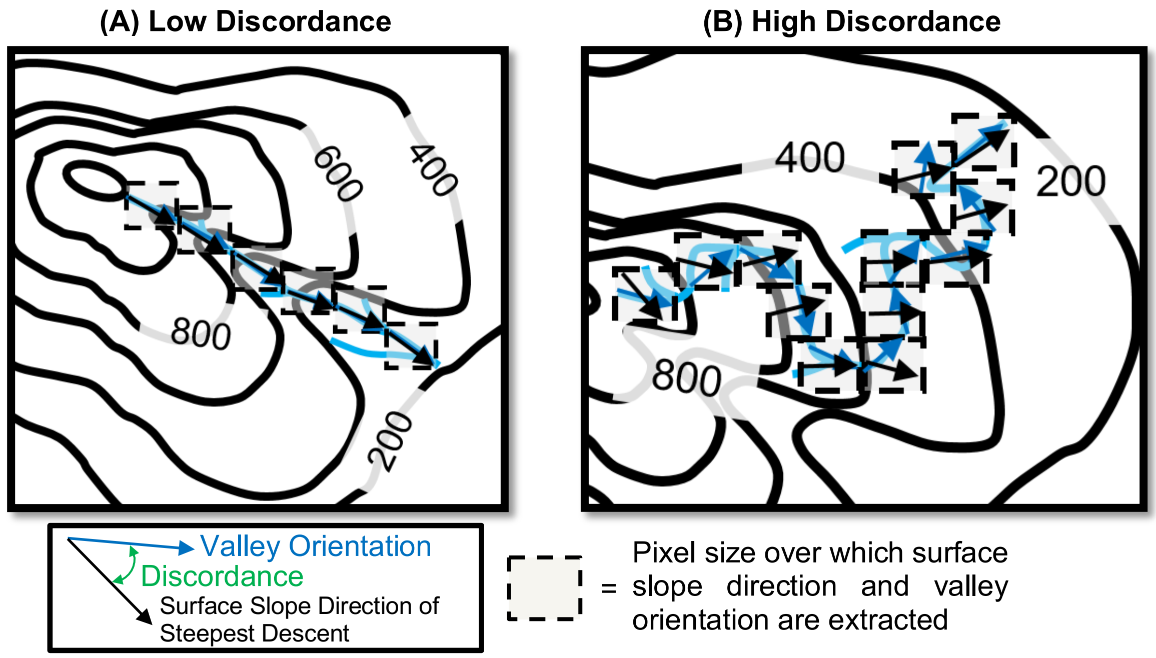


**Figure 1.** This figure is taken from Bahia et al., (2022). Schematic of the concept of discordance, with the blue lines representing a valley network and the black lines are topographic contours. Discordance is the angular difference between valley orientation and surface slope direction of steepest descent. (A) and (B) show hypothetical examples of a valley with low and high discordance values respectively. In these examples, only the main valleys (the longest in the drainage network) have hypothetical discordance calculation; in this study, we perform discordance analysis on all valleys and tributaries.

For this a pole-to-pole strip located from 20°W - 20°E (Figure 1) was chosen, where tectonic activity associated with the Tharsis Rise and Dichotomy Boundary may have affected the valley networks, and where slopes have also been affected locally by meteorite impacts. In this strip a new high-resolution slope discordance map was generated using HRSC images to identify all currently exposed channels and valley systems that have been produced either directly or indirectly through precipitation run-off e.g., direct precipitation or melting of glacial headwaters. V-shaped incisional valley networks are by far the most abundant valley type. Focusing on these types of valley, it was shown show tighter constraints on tectonic timing, and the location, magnitude and causes of deformation, may be obtained by mapping the spatial distribution of discordance in valley network slopes. In addition, we will show that discordance analysis provides a means of identifying suitable candidate river systems for slope-dependent paleohydraulic reconstructions of the fluvial activity on Mars. Additionally, it was shown that the conformity between valley orientation and surface slope direction is scale dependent.

## 2.1 Acknowledgements

We would like to thank the NASA's Mars Express Context Camera and Mars Orbiter Laser Altimeter teams. We would also like to thank the ESA's Mars Express High-Resolution Stereo Camera team.

The HRSC images were obtained from the ESA's Planetary Science Archive (PSA): https://archives.esac.esa.int/psa/ftp/MARS-EXPRESS/HRSC/

The CTX images were obtained from the Mars Space Flight Facility Image Explorer: http://viewer.mars.asu.edu/viewer/ctx?fbclid=IwAR2GeG5pqU4-2VaVGT96rU05y-cqNzrbnYCqWt8a9j00wKOUCVOEcbxOKSM#T=0

The MOLA data was downloaded from the USGS Astropedia website: https://astrogeology.usgs.gov/search/map/Mars/GlobalSurveyor/MOLA/Mars_MGS_MOLA_DEM_mosaic_global_463m

If you use this dataset please reference "Bahia, R. S., S. Covey-Crump, M. A. Jones and Neil Mitchell (2022), Discordance analysis on a high-resolution valley network map of Mars: Assessing the effects of scale on the conformity of valley orientation and surface slope direction, Icarus, 383, 115041."

# 3. DATA PRODUCT GENERATION

Much of the information in this section is taken from Bahia et al., (2022).

The valley and inverted channel map was generated in this study from ESA Mars Express Orbiter – HRSC images (~15 to 25 m per pixel). These images are available on the Mars Express HRSC and VMC (Visual Monitoring Camera) Images website (http://open.esa.int/mars-express-hrsc-and-vmc-images/) and USGS PILOT Website (https://pilot.wr.usgs.gov). The HRSC images cover ~96 % of the Martian surface [Neukum et al., 2004]. Where HRSC images were not available or corrupted CTX (Context Camera) images at a resolution of ~ 5 m per pixel were employed. CTX images were also used in the few areas where HRSC coverage was not present. Images were projected using a combination of ISIS 3 (Integrated Software for Imagers and Spectrometers) and the United States Geological Survey (USGS) Map Projection Web Service (POW) image processing cloud to generate ArcMap 10.2.1 readable ".cub" file formats. A total of 449 HRSC and 21 CTX images were processed and utilised in this study. For the present-day topography we used the Mars MGS MOLA DEM 463m (MOLA DEM), created using information from the Mars Orbiter Laser Altimeter (MOLA [Smith et al., 2001]), with a horizontal resolution of ~463 m per pixel at the equator and, due to the global error in the areoid (±1.8 meters; [Neumann et al., 2001]), ~3 m vertical precision [Lemoine et al., 2001]. The ages and geological units of the surfaces dissected by the mapped valleys and inverted channels were obtained using the Atlas of Mars 1:15,000,000-Scale Global Geologic Series Map [Skinner et al., 2006], in which the surface ages have been determined from crater density counts. As incisional valley networks are the focus of this study, their age distribution was further scrutinised using the higher resolution surface age map of Tanaka et al. [2014].

The valleys and inverted channels were identified, independent of previous valley maps, and their morphology assessed using ArcMap 10.2.1, with each of the 449 HRSC images examined individually. The valleys and inverted channels were manually mapped as vector-based lines, using the polyline function within ArcMap. As in previous studies [Carr, 1995; Scott et al., 1995; Hynek et al., 2010], valleys were identified as sublinear, incisional features, many of which form branching networks that slightly increase in size downstream and divide into smaller branches upslope. All visible valleys and tributaries were mapped for each network. To validate these sublinear features as valleys, the ArcMap Interpolate Line feature was used to produce cross-sections of any valley with a width greater than ~1 km as the images were being analysed. This also allowed the morphologies of the valleys to be examined. All channels identified in this study were inverted (e.g., Figures 7, 9 and 10), that is, they appear as ridges left behind by preferential erosion of the river banks and flood plains after the fluvial system became inactive [e.g., Williams et al., 2009; Burr et al. 2010; Davis et al., 2016]. Valleys were not connected into networks unless the junctions were visible. Where valleys encounter an obstacle such as a crater, the valleys on either side of that obstacle were only connected if the obstacle was smaller than the valley width or the valley could unambiguously be seen to dissect or run into and out of the obstacle. To eliminate gullies that could have been formed by mass wasting processes, valleys with longitudinal slopes of >10° were removed [Pilorget and Forget, 2016; Sylvest et al. 2018].

From the valley and inverted channel map we created, we have calculated valley and channel length, valley slope and drainage density of incisional valleys for comparison with previous studies. The lengths were determined using a combination of ArcMap tools. The Editor Tool was used to trace polylines along the centres of the features. Each polyline represents a valley or inverted channel segment within a network with its start and end point based on its Horton stream order [Horton, 1945]. Under the Horton [1945] stream order scheme, first-order valleys are those which have no tributaries, second-order valleys only receive first order valleys, etc. The main valley is denoted by the same order number from its source to termination, and hence one of the first-order streams (commonly the most direct or longest upstream continuation of the main stream) has to be renumbered to that of the main valley (e.g., Figure 2). The lengths of the polylines were calculated using the Calculate Geometry function.

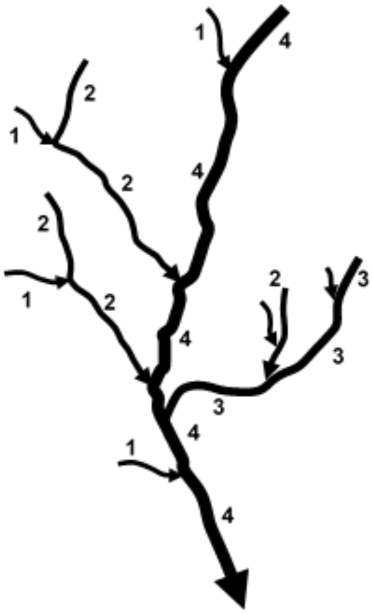


Figure 2. This figure is taken from Bahia et al., (2022). Example of Horton's stream order. The arrows point in the direction of hypothesised valley orientation based on the network's geometry. Line thickness increases with increasing Horton stream order.

To find areas of discordance the present-day topographic slope direction of steepest descent ($\theta$) and valley orientations ($\Psi$) were measured. The procedure for calculating $\Psi$ and $\theta$ follows and develops on that of Luo and Stepinski [2012]. The ArcMap 10.2.1 Spatial Analyst – Aspect tool (e.g., Figure 3A), which calculates the azimuthal direction of steepest descent for each square shaped pixel, was used to convert the DEMs into maps of $\theta$. This was performed on several DEMs of varying resolution (463 m, 1 km, 10 km and 50 km per pixel), so that we could compare $\Psi$ with $\theta$ at a range of scales. Craters were not removed from these DEMs before $\theta$ calculations were performed; many craters on Mars have both external and internal rims that are dissected by valley networks, meaning their interiors define the topographic slope directions on which valleys form. Extreme examples of this are valleys in pit craters [e.g., Peel and Fassett, 2013]. $\theta$ values were extracted every 463m down each valley and tributary (Figure 3B). For the few valleys/tributaries shorter than 463m in length, data was extracted from a central point. All values were averaged for each valley/tributary to give an average $\theta$ value for that valley/tributary. In this way, all valleys and tributaries were assigned their own individual $\theta$ value at each DEM resolution.

Unlike the previous technique [Luo and Stepinski, 2012] where $\Psi$ values were calculated as the orientation between the beginning and end point of a valley/tributary, we calculate $\Psi$ by converting the polylines into compass directions pointing in the direction of valley segment orientation every 463 m (Figure 3C). For the few valleys/tributaries shorter than 463m in length, the orientation was calculated as the direction between the beginning and end point. This was done using the ArcMap *Spatial Analyst - Linear Direction Mean* function. These values were then averaged resulting in an average $\Psi$ for each valley/tributary (Figure 3D). These $\Psi$ depend upon the direction (source to termination/termination to source for the main valley, or source to confluence/confluence to source for tributaries) in which the polylines were traced. To establish that the polylines were being traced consistently from source to termination/confluence and not vice versa, the following working rule (as used in previous Martian valley mapping studies [e.g., Carr, 1995; Hynek et al., 2010]) was applied: upslope the valleys are small, branched, sublinear incisional features which merge downstream to form a singular entity that increases in size (Figure 3). Determining $\Psi$ therefore relies on the presence of small valleys running into larger valleys. In rare cases where the valley lacks tributaries, the valley direction was taken to be in the same general direction as proximal adjacent valley networks. If adjacent valleys were absent, the valley was traced in the direction of increasing valley width [Montgomery and Gran, 2001]. The values of $\theta$ and $\Psi$ were specified relative to SimpleCylindrical_Mars grid north, i.e., $\theta$ (or $\Psi$) = 0° = 360° if the polyline pointed directly north. We define the magnitude of discordance ($D$) for each valley as the difference between $\Psi$ and $\theta$, that is, $D = |\Psi - \theta|$. This results in a $D$ value for all main valleys and tributaries.

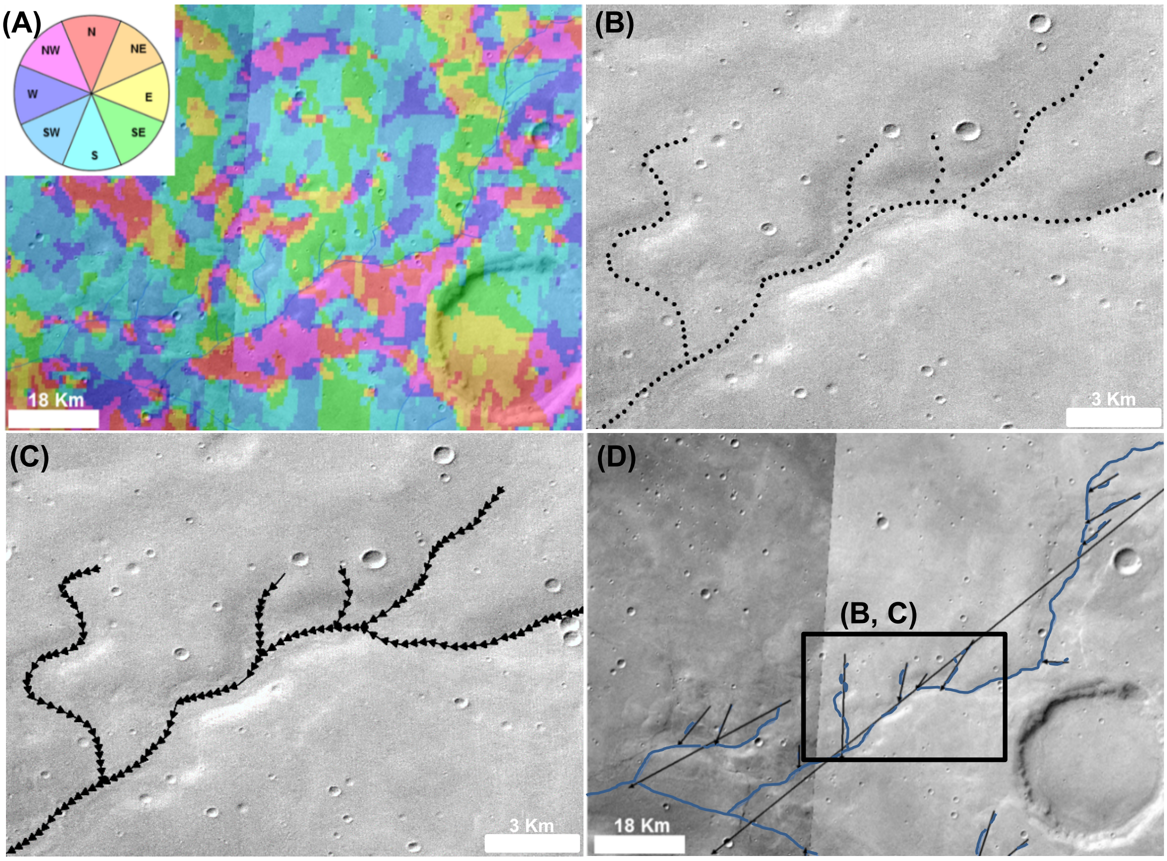


**Figure 3.** This figure is taken from Bahia et al., (2022). Example image located east of Vogel Crater (lat. 35.8°S, long. 8.9°W) of (A) present-day regional slope direction of steepest descent ($\theta$) generated from the 463 m per pixel DEM; (B) points, separated by 463m, at which $\theta$ was extracted along the valleys; (C) valley segment orientation every 463 m shown as black arrows; (D), taken from Bahia and Jones [2020], averaged valley orientation for each valley/tributary of a given Horton stream order within that network ($\Psi$) shown as the straight black lines overlain on the blue valleys. The black rectangle represents the footprint of (B) and (C).

Additionally, considering the scale over which a valley is likely to conform to $\theta$ is length dependent [e.g., Lipp and Roberts, 2020], and issues that may arise in extracting $\theta$ values (Figure 5, a map of ***scale dependent*** discordance ($D_{SD}$) was produced. For this, the $\Psi$ was compared to $\theta$, with the scale of the $\theta$ varying based on the length of the valleys/tributaries ($\theta_{SD}$). Specifically, for valleys/tributaries<1.5 km in length, the $\theta$ was calculated at MOLA

DEM resolution (463m – $\theta_{463m}$). For valleys/tributaries between 1.5 km and 20 km in length, the 1km DEM was used ($\theta_{1km}$). This is because valley/tributaries between these lengths often have widths greater than 463m. For valleys/tributaries >20 km in length, the 10km DEM was used ($\theta_{10km}$). Similar to the former, these valleys/tributaries often have widths > 1km. Finally, several large valleys (>300 km in length) have widths greater than 10km. For these, the 50km DEM was used ($\theta_{50km}$).

The dataset was reviewed and accepted for publication in the academic journal, Icarus.

# 4. ARCHIVE FORMAT AND CONTENT

The dataset consists of 5 shape files (.shp) and their georeference metadata (.cpg, .dbf, .prj, .sbn, .sbx, .shx and .shp.xml).
They are as follows:

- Bahia_et_al_Valleys.shp, Bahia_et_al_Valleys.cpg, Bahia_et_al_Valleys.dbf, Bahia_et_al_Valleys.prj, Bahia_et_al_Valleys.sbn, Bahia_et_al_Valleys.sbx, Bahia_et_al_Valleys.shx and Bahia_et_al_Valleys.shp.xml
- Bahia_et_al_Valleys_of_Uncertain_Origin.shp, Bahia_et_al_Valleys_of_Uncertain_Origin.cpg, Bahia_et_al_Valleys_of_Uncertain_Origin.dbf, Bahia_et_al_Valleys_of_Uncertain_Origin.prj, Bahia_et_al_Valleys_of_Uncertain_Origin.sbn, Bahia_et_al_Valleys_of_Uncertain_Origin.sbx, Bahia_et_al_Valleys_of_Uncertain_Origin.shx and Bahia_et_al_Valleys_of_Uncertain_Origin.shp.xml
- Bahia_Inverted_Channel–Sinuous.shp, Bahia_Inverted_Channel–Sinuous.cpg, Bahia_Inverted_Channel–Sinuous.dbf, Bahia_Inverted_Channel–Sinuous.prj, Bahia_Inverted_Channel–Sinuous.sbn, Bahia_Inverted_Channel–Sinuous.sbx, Bahia_Inverted_Channel–Sinuous.shx and Bahia_Inverted_Channel–Sinuous.shp.xml
- Bahia_Inverted_Channel–Straight.shp, Bahia_Inverted_Channel–Straight.cpg, Bahia_Inverted_Channel–Straight.dbf, Bahia_Inverted_Channel–Straight.prj, Bahia_Inverted_Channel–Straight.sbn, Bahia_Inverted_Channel–Straight.sbx, Bahia_Inverted_Channel–Straight.shx and Bahia_Inverted_Channel–Straight.shp.xml
- Bahia_Inverted_Channel–Multithread.shp, Bahia_Inverted_Channel–Multithread.cpg, Bahia_Inverted_Channel–Multithread.dbf, Bahia_Inverted_Channel–Multithread.prj, Bahia_Inverted_Channel–Multithread.sbn, Bahia_Inverted_Channel–Multithread.sbx, Bahia_Inverted_Channel–Multithread.shx and Bahia_Inverted_Channel–Multithread.shp.xml

.shp = The vector data storage format that stores the feature geometry.
.shx = The index file that stores the index of the feature geometry.

.dbf = The dBASE table that stores the attribute information of features.

.sbn and .sbx = The files that store the spatial index of the features.
.prj = The file that stores the coordinate system information.
.cpg = An (optional) file that can be used to specify the codepage for identifying the characterset to be used.
.shp.xml = the file that is the geospatial metadata in XML format.

The best software packages to interrogate the software are GIS (e.g., ArcGIS or QGIS). Accessing the data only requires the user to drag and drop the shape file (.shp) into the chosen GIS software.

Data within the shape files can be accessed by right-clicking on the shape file name within the contents panel and opening the attribute table.

The shapefiles contain the following information:

| | FID | Shape | Scaled_D | Scaled_θ | Ψ | Length_m |
|---|---|---|---|---|---|---|
| | Description | | | | | |
| Shp. File Name | Feature number. | Type of shapefile (i.e., polyline, point or polygon). | Difference between Scaled_θ and Ψ. | Average surface slope direction (°) extracted from scales adjusted based on valley length. | Valley orientation (°). | Feature length in metres. |
| Bahia_et_al_Valleys | X | X | X | X | X | X |
| Bahia_et_al_Valleys_of_Uncertain_Origin | X | X | | | | X |
| Bahia_Inverted_Channel–Sinuous | X | X | | | | X |
| Bahia_Inverted_Channel–Straight | X | X | | | | X |
| Bahia_Inverted_Channel–Multithread | X | X | | | | X |

# KNOWN ISSUES

Much of the information in this section is taken from Bahia et al., (2022).

Where the valley floor is difficult to discern, the traced polyline may mistakenly be drawn up the valley wall (Figure 4). This introduces an error into calculated $\Psi$ and, more significantly, it introduces an error into the $\theta$ as calculated along the misplaced polyline (e.g., compare the true $\theta$ with the calculated $\theta$ in Figure 4). This can result in a valley that conforms to topography being incorrectly identified as having a discordance of anything up to 90°. Considering $\theta$ values were averaged along each valley, this error only significantly affects the results if the polylines are mistakenly traced along one of the valley walls preferentially. However, a similar issue may arise if the scale over which $\theta$ is calculated is smaller than that of the valley width, as topographic modifications along the valley floor (e.g., due to valley wall slumping and/or aeolian deposition and erosion) can cause the local slope direction to not be representative of the underlying valley floor. The aforementioned effects are not significant for valleys with widths smaller than the pixel size over which $\theta$ is extracted.

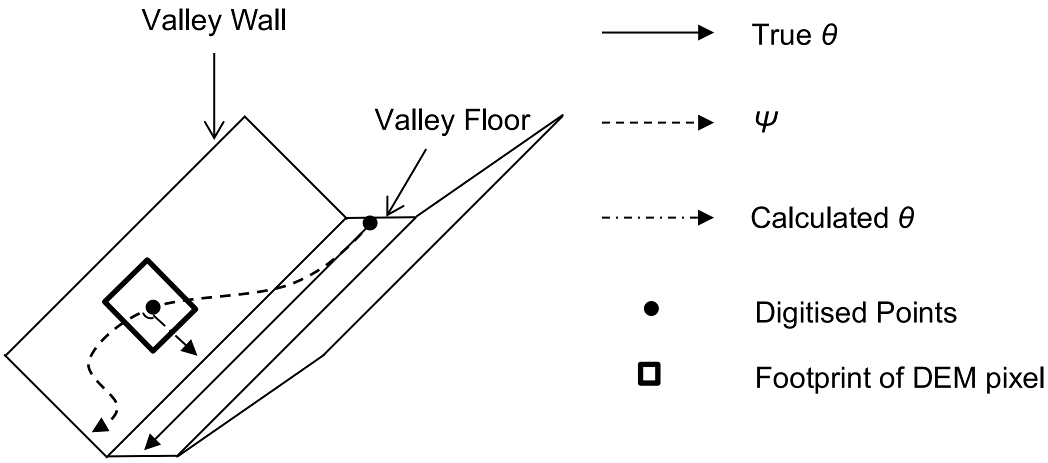


**Figure 4.** The effects of mistakenly locating the polyline for a concordant valley ($\theta = \Psi$) on the discordance analysis. The polyline is here shown mounting the valley wall rather than following the valley floor – in this case the calculated slope direction is at ~90° to the true slope direction.

It should also be noted that there is subjectivity when tracing valley networks [Bahia and Jones, 2020], which will affect the obtained values of $\Psi$. To gain some understanding of this affect, a repeatability study was conducted. This was carried out by the same observer (Bahia) mapping valleys between 26.75°S, 16.97°W and 36.86°S, 5.27°W twice, with a two year gap between. 1548 valleys were mapped in total. The polylines were converted into vectors, representative of $\Psi$ (Figure 5), and the difference between the values of $\Psi$ for corresponding polylines was calculated. We find the uncertainty in $\Psi$ that arises from our uncertainty in the tracing of valleys is ~ ± 12° (1 standard deviation).

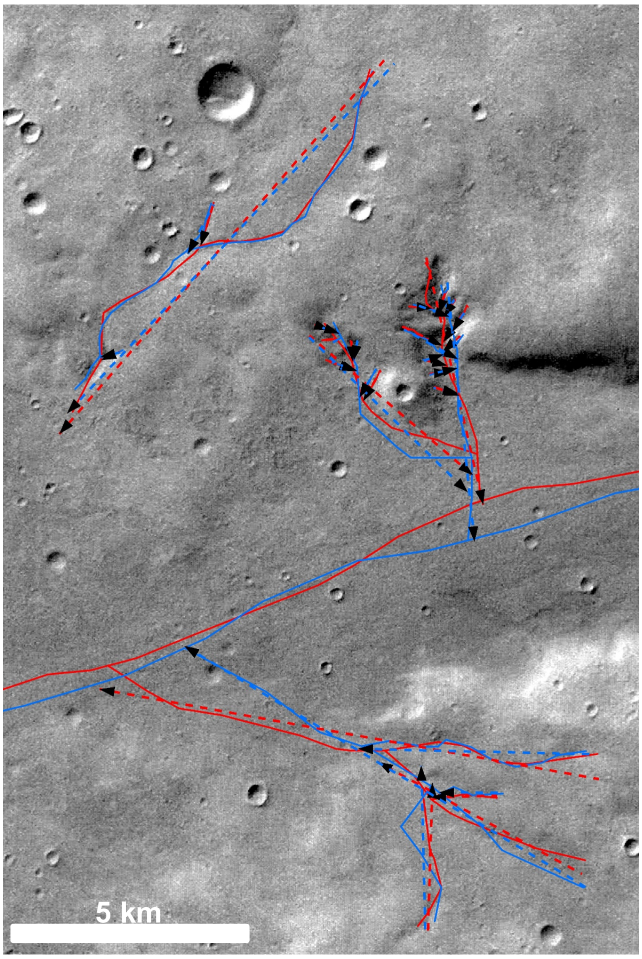


**Figure 5.** Example of the repeatability analysis used to establish our uncertainty on paleoslope direction (HRSC images: h8592_0000). The earlier of our valley maps is shown by red polylines and the second valley map created is shown in blue. In each case, the dashed lines show the averaged $\Psi$ for a given valley/tributary. In this example, the mean difference between the $\Psi$ values obtained from the two maps is ~8°.

# 5. SOFTWARE

The best software packages to interrogate the data are GIS (e.g., ArcGIS or QGIS). Accessing the data only requires the user to drag and drop the shape file (.shp) into the chosen GIS software